Nonlinear Dyn (2019) 96:1541–1557
https://doi.org/10.1007/s11071-019-04870-5

ORIGINAL PAPER

Development and experimental investigation of a Quadrotor's robust generalized dynamic inversion control system

Uzair Ansari · Abdulrahman H. Bajodah · Belkacem Kada

Received: 1 August 2018 / Accepted: 28 February 2019 / Published online: 8 March 2019

Abstract The development of a two-loops Quadrotor's robust generalized dynamic inversion (RGDI)-based control system is presented. The outer (position) loop utilizes PD position control of the Quadrotor's center of gravity (CG) in the three-dimensional inertial space, and it provides reference pitch and roll tilting angles commands to the inner loop, in addition to the thrust command that is required to track desired altitude trajectories. The inner (attitude) loop applies RGDI control of a prescribed asymptotically stable dynamics of tilting and attitude errors from reference-tilting and desired-attitude trajectories, and it provides the three required control torque values such that desired CG positions in instantaneous horizontal inertial planes and desired-attitude trajectories of the Quadrotor are tracked. The proposed closed loop system is shown to guarantee finite-time semi-global practically stable trajectory tracking. Numerical simulations of the proposed closed loop control system are performed on a six degrees of freedom Quadrotor's mathematical model for nominal conditions and under parametric uncertainties and exogenous disturbances. Apart from numerical simulations, experimental tests are conducted on a three degrees of freedom Quadrotor test bench to assess performance of the RGDI control loop. Experimental results demonstrate improved tracking performance in comparison with classical Linear-Quadratic optimal control and conventional sliding mode control.

Keywords Robust generalized dynamic inversion · Sliding mode control · Quadrotor control · Hover experimental test bench · Null control vector · Trajectory tracking · Finite-time stability · Semi-global practical stability

U. Ansari · A. H. Bajodah (✉) · B. Kada
Aeronautical Engineering Department, King Abdulaziz University, P.O. Box 80204, Jeddah 21589, Saudi Arabia
e-mail: abajodah@kau.edu.sa

U. Ansari
e-mail: uzansari@hotmail.com

B. Kada
e-mail: bkada@kau.edu.sa

1 Introduction

The Quadrotor is a six degrees of freedom (DoF) unmanned rotorcraft vehicle that is becoming increasingly popular in industrial, commercial, and military applications because of its favorable capabilities. These capabilities include Vertical Take-Off and Landing (VTOL) and the hovering ability.

The Quadrotor's structure is simple compared to other types of rotorcraft. For the purpose of torque balancing the vehicle and controlling its motion, it is equipped with four rotors that are cross configured such that one pair of rotors rotates in one direction, while the other pair rotates in the opposite direction. The Quadrotor's motion in the three-dimensional space in addition to the Quadrotor's attitude are controlled by changing the thrust forces of the rotors.

The Quadrotor has been displaying a wide range of applications. These applications include mapping and surveillance, search and rescue support, object grasping and handling, atmospheric measurements, agricultural services, marine operations, education and scientific research, entertainment, and several other potential applications, see [1] for a survey.

The fast expanding in the Quadrotor's applications and the need to operate it in harsh and uncertain environments caused new control system design challenges to rise for this type of flying robots. Moreover, the inherent characteristics of the Quadrotor adds more complexities and difficulties in the way to design robust control systems for its missions. These characteristics include under-actuation, the coupled and highly nonlinear system dynamics, in addition to dynamic and aerodynamic modeling uncertainties, see, e.g., [2,3].

Among the model-based control design methodologies that have been used to control quadrotors are linear methodologies [4–6], e.g., [7–11], backstepping control [12–14], e.g., [11,15], sliding mode control (SMC) [16–21], e.g., [22–31], feedback linearization by nonlinear dynamic inversion (NDI) [16,18], e.g., [31–33], and geometric control [34,35], e.g., [36–38], see [39] for a survey.

Generalized dynamic inversion (GDI) [40,41] is a constrained control design methodology that utilizes the Moore–Penrose generalized inverse (MPGI) [42,43] and the associated null space parametrization of nonsquare matrices [44–46]. Similar to its preceding NDI control methodology [47–49], GDI has been evolving within aerospace control applications, e.g., [50–56]. However, GDI control avoids the main limitations and shortcomings of NDI in its implementations to control complex and highly nonlinear aerospace systems [30]. The null control vector [40,41] that is involved in the GDI control law provides a design freedom that allows to augment GDI with other control design methodologies to enhance the GDI control design [30].

The GDI control methodology is of the left inversion type, i.e., the control inputs are obtained by means of plant's output's error feedback and not based on actual plant's outputs. Therefore, GDI control does not involve deriving inverse dynamical equations of motion for the controlled plant. Instead, prescribed servo (virtual) constraints that represent the control objectives are evaluated along the trajectories of the open loop dynamical system and are imposed thereafter on its closed loop dynamics by means of the MPGI-based Greville formula.

The Quadrotor dynamics is of a two time scales nature because the Quadrotor's attitude dynamics is much faster than its translational dynamics. Since the two-loops control system structure has shown effective for controlling dynamical systems in this nature, it has been a tradition to utilize that structure for Quadrotor control. In reference [30], the outer positional (slow) loop is controlled via a robust version of GDI that is designed by augmenting an additional SMC loop within the classical GDI control system, and Nonsingular Terminal SMC was applied to inner attitude (fast) loop.

This paper shows that the Quadrotor's inner fast dynamics can be controlled as efficiently by utilizing robust GDI (RGDI). A linear Proportional-Derivative (PD) state feedback control of inertial position errors is applied in the outer positional loop to generate reference pitch and roll tilting profiles, along with generating the required thrust force command to track desired altitude trajectories. The inner attitude loop employs RGDI control . The inner loop aims to steer the tilting and attitude angles toward their reference-tilting and desired-attitude trajectories by generating the required control thrust moment commands. The RGDI control system guarantees finite-time practically semi-globally stable Quadrotor's attitude trajectory tracking, and it provides performance robustness against unmodeled dynamics, parametric variations and uncertainties, and bounded external disturbances, in addition to robustness against tracking performance deterioration due to MPGI dynamic scaling.

The null control vector in the auxiliary part of the RGDI control law is designed in this paper to stabilize the inner dynamics of the Quadrotor, and it is chosen to be linear in the body angular velocity components. The proportionality gain matrix is constructed via a control Lyapunov function, and the null control design is shown to guarantee global closed loop asymptotic stability of the Quadrotor's angular velocity dynamics. Orthogonality of the particular and the auxiliary control subspaces of the RGDI control law ensures noninterference of the attitude tracking and the inner dynamics stabilization control actions, and thus, it ensures that both actions work toward a unified goal, and work to reduce the total control effort.

To assess the effectiveness of the proposed control system design, numerical simulations are conducted

on a six DoF mathematical model of a three DoF experimental Hovering system, in both nominal and perturbed flight conditions. Performance of the inner RGDI attitude control loop is further assessed by performing laboratory experiments on a three DoF hovering test bench, and RGDI attitude control performance is compared with that of classical LQR and conventional SMC, showing superiority of RGDI control.

The remaining sections of the paper are organized as following: A dynamic modeling brief of the Quadrotor is given in Sect. 2, and the proposed two-loops baseline control system structure is illustrated in Sect. 3. A small disturbance linearization-based PD control design for the outer positional loop is made in Sect. 4. The RGDI detailed design procedure for the inner attitude control loop is presented in Sect. 5, including formulation of the dynamical constraint, the null control vector design, integration of the SMC control element, and a proof of the guaranteed finite-time semi-global practically stable attitude tracking performance of the inner RGDI control loop. The numerical simulations and the experimental results are presented in Sect. 6, and concluding remarks are given in Sect. 7.

2 Quadrotor mathematical modeling

The Quadrotor's main frame is assumed to be a rigid body, and its center of gravity (CG) is assumed to coincide with the origin $O_{\mathbf{B}}$ of the body coordinate system. The Quadrotor's body-fixed reference frame is denoted by $\boldsymbol{B}(x_b, y_b, z_b)$, and the inertial Earth-fixed reference frame is denoted by $\boldsymbol{E}(x_e, y_e, z_e)$ as shown in Fig. 1. The total Quadrotor's thrust force in the negative z_b direction is given by

$$T = \sum_{i=1}^{4} T_i = b \sum_{i=1}^{4} \omega_i^2, \quad i = 1, 2, 3, 4 \tag{1}$$

where T_i is the thrust force of the ith rotor in the negative z_b direction, b is the lift coefficient of an individual rotor and is assumed to be identical for the four rotors, and ω_i is angular speed of the ith rotor, and it is negative for $i = 1, 3$ and positive for $i = 2, 4$. The torques generated by the rotors about the x_b axis (τ_x rolling torque), y_b axis (τ_y pitching torque), and z_b axis (τ_z yawing torque) are given by

$$\tau_x = db(\omega_4^2 - \omega_2^2) \tag{2}$$

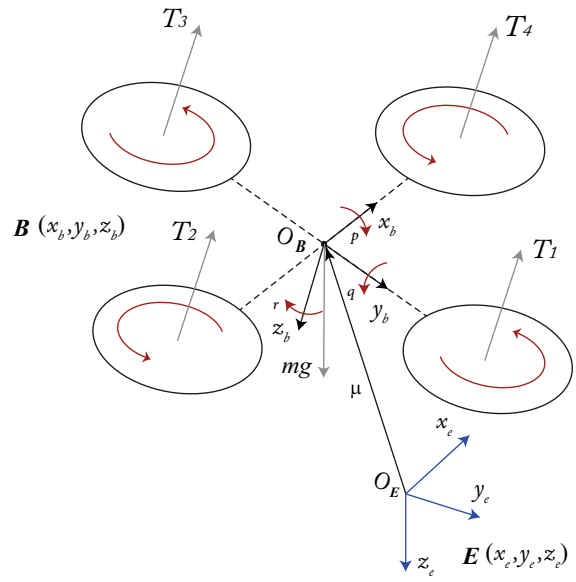

Fig. 1 Quadrotor configuration

$$\tau_y = db(\omega_3^2 - \omega_1^2) \tag{3}$$

$$\tau_z = k(\omega_1^2 - \omega_2^2 + \omega_3^2 - \omega_4^2) \tag{4}$$

where d is the moment arm of T_i about $O_{\mathbf{B}}$, $i = 1, \ldots, 4$. The yawing moment τ_z that is given by (4) is generated by the rotors' drag forces that tend to rotate the Quadrotor in opposite directions by creating reaction torques on the Quadrotor's body, where the drag-to-moment coefficient k is determined experimentally [2,57]. The Quadrotor is an under-actuated dynamical system having a 4-dimensional input vector

$$\boldsymbol{u} = \begin{bmatrix} T & \tau_x & \tau_y & \tau_z \end{bmatrix}^{\mathrm{T}} \tag{5}$$

and a twelve-dimensional controlled state vector

$$\boldsymbol{x} = \begin{bmatrix} x_e & y_e & z_e & \dot{x}_e & \dot{y}_e & \dot{z}_e & \phi & \theta & \psi & \dot{\phi} & \dot{\theta} & \dot{\psi} \end{bmatrix}^{\mathrm{T}} \tag{6}$$

where ϕ, θ, and ψ are, respectively, Euler's roll, pitch, and yaw angles that are used as coordinates of angular orientation [58]. The relation between the input vector $\boldsymbol{u}$ and the angular speeds of the rotors is given by [2]

$$\boldsymbol{u} = \boldsymbol{R} \begin{bmatrix} \omega_1^2 & \omega_2^2 & \omega_3^2 & \omega_4^2 \end{bmatrix}^{\mathrm{T}} \tag{7}$$

where $\boldsymbol{R}$ is the 4×4 full rank constant matrix given by

$$\boldsymbol{R} = \begin{bmatrix} -b & -b & -b & -b \\ 0 & -db & 0 & db \\ \mathrm{d}b & 0 & -db & 0 \\ k & -k & k & -k \end{bmatrix}. \tag{8}$$

The translational Quadrotor's kinematics in $\boldsymbol{E}$ is given by the vector equation

$$\dot{\boldsymbol{\mu}} = \boldsymbol{v} = \begin{bmatrix} \dot{x}_e & \dot{y}_e & \dot{z}_e \end{bmatrix}^{\mathrm{T}} \tag{9}$$

where $\boldsymbol{\mu}$ and $\boldsymbol{v}$ are the inertial displacement and velocity vectors of the Quadrotor's center of gravity $O_{\mathbf{B}}$, respectively. The translational Quadrotor's dynamics are modeled by Newton's equations of motion

$$m \frac{^{\boldsymbol{E}}\mathrm{d}\boldsymbol{v}}{\mathrm{d}t} = mg\boldsymbol{n}_{\boldsymbol{E}} - T\boldsymbol{n}_{\boldsymbol{B}} \tag{10}$$

where m is the Quadrotor's mass, g is the acceleration due to gravity, and

$$\frac{^{\boldsymbol{E}}\mathrm{d}\boldsymbol{v}}{\mathrm{d}t} = \dot{\boldsymbol{v}} = \begin{bmatrix} \ddot{x}_e & \ddot{y}_e & \ddot{z}_e \end{bmatrix}^{\mathrm{T}} \tag{11}$$

is the time derivative of $\boldsymbol{v}$ relative to $\boldsymbol{E}$, and the unit vectors $\boldsymbol{n}_{\boldsymbol{E}}$ and $\boldsymbol{n}_{\boldsymbol{B}}$ are in the positive z_e and z_b directions, respectively. Expressing (10) in $\boldsymbol{E}$ and solving for the inertial accelerations $\ddot{x}_e$, $\ddot{y}_e$, and $\ddot{z}_e$ yield

$$\begin{bmatrix} \ddot{x}_e \\ \ddot{y}_e \\ \ddot{z}_e \end{bmatrix} = \begin{bmatrix} 0 \\ 0 \\ g \end{bmatrix} - \boldsymbol{L}_{\boldsymbol{EB}} \begin{bmatrix} 0 \\ 0 \\ \frac{T}{m} \end{bmatrix} \tag{12}$$

where $\boldsymbol{L}_{\boldsymbol{EB}}$ is the $L_x(-\phi) \rightarrow L_y(-\theta) \rightarrow L_z(-\psi)$ transformation matrix from $\boldsymbol{B}$ to $\boldsymbol{E}$, see, e.g., [58]. The final form of (12) is

$$\begin{bmatrix} \ddot{x}_e \\ \ddot{y}_e \\ \ddot{z}_e \end{bmatrix} = \begin{bmatrix} 0 \\ 0 \\ g \end{bmatrix} - \begin{bmatrix} s_\psi s_\phi + c_\psi s_\theta c_\phi \\ -c_\psi s_\phi + s_\psi s_\theta c_\phi \\ c_\theta c_\phi \end{bmatrix} \frac{T}{m} \tag{13}$$

where the abbreviations c_ψ and s_θ refer to $\cos\psi$ and $\sin\theta$, etc. Denote the angular velocity vector of $\boldsymbol{B}$ with respect to $\boldsymbol{E}$ by $\boldsymbol{\Omega}$, and express it in $\boldsymbol{B}$ as

$$\boldsymbol{\Omega} = \begin{bmatrix} p & q & r \end{bmatrix}^{\mathrm{T}} \tag{14}$$

and denote the angular velocity vector of the ith rotor with respect to $\boldsymbol{E}$ by $\boldsymbol{\Omega}_{\boldsymbol{r}_i}$, and express it in $\boldsymbol{B}$ as

$$\boldsymbol{\Omega}_{\boldsymbol{r}_i} = \begin{bmatrix} p & q & r + \omega_i \end{bmatrix}^{\mathrm{T}}. \tag{15}$$

The Quadrotor's rotational kinematics is given by the relation between the time rates of Euler's angles and the body components of $\boldsymbol{\Omega}$ as [58]

$$\begin{bmatrix} \dot{\phi} \\ \dot{\theta} \\ \dot{\psi} \end{bmatrix} = \begin{bmatrix} 1 & s_\phi t_\theta & c_\phi t_\theta \\ 0 & c_\phi & -s_\phi \\ 0 & s_\phi / c_\theta & c_\phi / c_\theta \end{bmatrix} \begin{bmatrix} p \\ q \\ r \end{bmatrix} \tag{16}$$

where t_θ stands for $\tan\theta$. Equation (16) is rewritten compactly as

$$\dot{\boldsymbol{\Psi}} = \boldsymbol{\Gamma}(\phi, \theta)\boldsymbol{\Omega}. \tag{17}$$

The angular momentum vector of the Quadrotor about $O_{\mathbf{B}}$ is

$$\boldsymbol{H} = \boldsymbol{J}\boldsymbol{\Omega} + \boldsymbol{J}_{\boldsymbol{r}} \sum_{i=1}^{4} \boldsymbol{\Omega}_{\boldsymbol{r}_i} \tag{18}$$

where $\boldsymbol{J} = \mathrm{diag}\begin{bmatrix} J_x, & J_y, & J_z \end{bmatrix}$ is the 3×3 Quadrotor's main frame's diagonal inertia matrix, such that J_x, J_y, and J_z are the principal moments of inertia constants, and $\boldsymbol{J}_{\boldsymbol{r}} = \mathrm{diag}\begin{bmatrix} 0, & 0, & J_{\mathrm{r}} \end{bmatrix}$ is the approximate 3×3 rotor's diagonal inertia matrix, where J_{r} is the rotor's polar moment of inertia constant about the rotor's axis of rotation, and is assumed identical for the four rotors, and the rotor's transverse moments of inertia constants about the axes in the plane of rotor's rotation are assumed ignorably small. The time derivative of $\boldsymbol{H}$ relative to $\boldsymbol{E}$ is given by the basic (transport) kinematical equation [59] as

$$\begin{aligned} \frac{^{\mathbf{E}}\mathrm{d}\boldsymbol{H}}{\mathrm{d}t} &= \frac{^{\mathbf{B}}\mathrm{d}\boldsymbol{H}}{\mathrm{d}t} + \boldsymbol{\Omega} \times \boldsymbol{H} \\ &= \boldsymbol{J}\dot{\boldsymbol{\Omega}} + \boldsymbol{\Omega}^{\times}\boldsymbol{J}\boldsymbol{\Omega} + \boldsymbol{J}_{\boldsymbol{r}} \sum_{i=1}^{4} \dot{\boldsymbol{\Omega}}_{\boldsymbol{r}_i} \\ &\quad + \boldsymbol{\Omega}^{\times}\boldsymbol{J}_{\boldsymbol{r}} \sum_{i=1}^{4} \boldsymbol{\Omega}_{\boldsymbol{r}_i} \end{aligned} \tag{19}$$

where $\dot{\boldsymbol{\Omega}} = \begin{bmatrix} \dot{p} & \dot{q} & \dot{r} \end{bmatrix}^{\mathrm{T}}$ and $\dot{\boldsymbol{\Omega}}_{\boldsymbol{r}_i} = \begin{bmatrix} \dot{p} & \dot{q} & \dot{r} + \dot{\omega}_i \end{bmatrix}^{\mathrm{T}}$ are, respectively, the time derivatives of $\boldsymbol{\Omega}$ and $\boldsymbol{\Omega}_{\boldsymbol{r}_i}$ relative to $\boldsymbol{B}$, and $\boldsymbol{\Omega}^{\times}$ is the cross product matrix that corresponds to $\boldsymbol{\Omega}$, and is given by

$$\boldsymbol{\Omega}^{\times} = \begin{bmatrix} 0 & -r & q \\ r & 0 & -p \\ -q & p & 0 \end{bmatrix}. \tag{20}$$

The rotational Quadrotor's dynamics are modeled by Euler's equations of motion

$$\frac{^{E}\mathrm{d}\boldsymbol{H}}{\mathrm{d}t} = \boldsymbol{\tau} \tag{21}$$

where $\boldsymbol{\tau} = \begin{bmatrix} \tau_x & \tau_y & \tau_z \end{bmatrix}^{\mathrm{T}}$. Substituting (19) in (21) and solving for $\dot{\boldsymbol{\Omega}}$ yields the following Quadrotor's rotational dynamical equations of motion in $\boldsymbol{B}$

$$\dot{\boldsymbol{\Omega}} = -\boldsymbol{J}^{-1}\left(\boldsymbol{\Omega}^{\times}\boldsymbol{J}\boldsymbol{\Omega} + \boldsymbol{J}_r\sum_{i=1}^{4}\dot{\boldsymbol{\Omega}}_{r_i} + \boldsymbol{\Omega}^{\times}\boldsymbol{J}_r\sum_{i=1}^{4}\boldsymbol{\Omega}_{r_i} - \boldsymbol{\tau}\right). \tag{22}$$

The acceleration form of Euler's kinematical equations (17) is derived next to have the control input appear in the equations. The time derivative of $\dot{\boldsymbol{\Psi}}$ is

$$\ddot{\boldsymbol{\Psi}} = \dot{\boldsymbol{\Gamma}}(\phi,\theta,\dot{\phi},\dot{\theta})\boldsymbol{\Omega} + \boldsymbol{\Gamma}(\phi,\theta)\dot{\boldsymbol{\Omega}} \tag{23}$$

where $\dot{\boldsymbol{\Gamma}}(\phi,\theta,\dot{\phi},\dot{\theta})$ is the element-wise time derivative of $\boldsymbol{\Gamma}(\phi,\theta)$. Substituting (22) in (23) yields the following compact expression for $\ddot{\boldsymbol{\Psi}}$

$$\ddot{\boldsymbol{\Psi}} = \boldsymbol{F} + \boldsymbol{G}\boldsymbol{\tau} \tag{24}$$

where

$$\boldsymbol{F} = \dot{\boldsymbol{\Gamma}}(\phi,\theta,\dot{\phi},\dot{\theta})\boldsymbol{\Omega} - \boldsymbol{\Gamma}(\phi,\theta)\boldsymbol{J}^{-1}\left(\boldsymbol{\Omega}^{\times}\boldsymbol{J}\boldsymbol{\Omega} + \boldsymbol{J}_r\sum_{i=1}^{4}\dot{\boldsymbol{\Omega}}_{r_i} + \boldsymbol{\Omega}^{\times}\boldsymbol{J}_r\sum_{i=1}^{4}\boldsymbol{\Omega}_{r_i}\right) \tag{25}$$

and

$$\boldsymbol{G} = \boldsymbol{\Gamma}\boldsymbol{J}^{-1}. \tag{26}$$

Moreover, because $|r| << |\omega_i|$ and $|\dot{r}| << |\dot{\omega}_i|$, (22) is approximated by omitting r and $\dot{r}$ in the expressions of $\boldsymbol{\Omega}_{r_i}$ and $\dot{\boldsymbol{\Omega}}_{r_i}$.

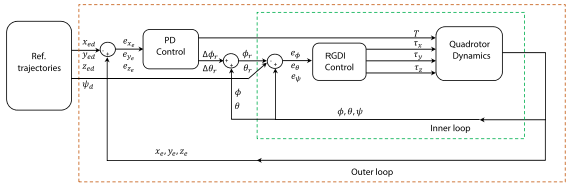

Fig. 2 PD-RGDI control system structure

3 Control system structure

The Quadrotor experiences a strong inherent coupling of pitch and roll dynamics. Moreover, the six DoF Quadrotor's controlled dynamics is actuated via four control thrusts, and therefore it is under-actuated by two degrees of actuation. Additionally, the Quadrotor's dynamics reveals a two time scales type of behavior since its attitude dynamics is much faster than its translational dynamics.

Hence, the control design philosophy that is adopted in the present work is based on controlling the Quadrotor's dynamics via two loops, outer and inner, as shown in Fig. 2. The outer (slow) loop controls the errors in the translational position variables, and it provides roll and pith tilting commands to the inner loop in addition to the thrust control variable that is required to track desired altitude trajectories. The inner (fast) loop controls the tilting and attitude error variables, and it provides the remaining three control (torque) variables.

Notice in Fig. 2 that the desired-attitude variable ψ_{d} that is produced by the reference trajectory generator bypasses the outer loop directly to the inner loop, and that the thrust control variable T outputs the outer loop's PD control block and bypasses the inner loop directly to the Quadrotor's dynamics block.

4 Outer PD control loop design

The PD outer control loop stabilizes the instantaneous horizontal inertial plane's position errors e_{x_e} and e_{y_e} by generating incremental reference tilting commands $\triangle\phi_r$ and $\triangle\theta_r$ that are added to the measured tilting angles ϕ and θ to produce the reference tilting angles commands ϕ_r and θ_r, respectively. For the purpose of generating these incremental commands, the nonlinear translational dynamics of x_e and y_e given by (13) are linearized about the instantaneous values of θ and ϕ by utilizing the small disturbance theory [58]. Accordingly, let ϕ_r and θ_r be given as

$$\phi_r(t) = \phi(t) + \triangle\phi_r(t) \tag{27}$$

and

$$\theta_r(t) = \theta(t) + \triangle\theta_r(t). \tag{28}$$

Expressions for the desired accelerations of O_B in the x_e and y_e directions are then obtained from (13) by replacing $\ddot{x}_e$ and $\ddot{y}_e$ by $\ddot{x}_{\text{ed}}$ and $\ddot{y}_{\text{ed}}$, and replacing ϕ and θ by the decomposed expressions of ϕ_r and θ_r given by (27) and (28) respectively, resulting in

$$\begin{bmatrix} \ddot{x}_{\text{ed}} \\ \ddot{y}_{\text{ed}} \end{bmatrix} = -\begin{bmatrix} s_\psi s_{(\phi+\triangle\phi_r)} + c_\psi s_{(\theta+\triangle\theta_r)} c_{(\phi+\triangle\phi_r)} \\ -c_\psi s_{(\phi+\triangle\phi_r)} + s_\psi s_{(\theta+\triangle\theta_r)} c_{(\phi+\triangle\phi_r)} \end{bmatrix} \frac{T}{m}. \tag{29}$$

Expanding the involved trigonometric functions about the instantaneous values $\phi(t)$ and $\theta(t)$ and applying the small disturbance theory assumptions yield the following linear system of equations in $\triangle\phi_r$ and $\triangle\theta_r$

$$\begin{bmatrix} \ddot{x}_{\text{ed}} \\ \ddot{y}_{\text{ed}} \end{bmatrix} = \boldsymbol{M}\boldsymbol{\delta} + \boldsymbol{N} \tag{30}$$

where

$$\boldsymbol{M} = -\frac{T}{m}\begin{bmatrix} s_\psi c_\phi - c_\psi s_\theta s_\phi & c_\psi c_\theta c_\phi \\ -c_\psi c_\phi - s_\psi s_\theta s_\phi & s_\psi c_\theta c_\phi \end{bmatrix} \tag{31}$$

$$\boldsymbol{N} = -\frac{T}{m}\begin{bmatrix} s_\psi s_\phi + c_\psi s_\theta c_\phi \\ -c_\psi s_\phi + s_\psi s_\theta c_\phi \end{bmatrix} \tag{32}$$

and

$$\boldsymbol{\delta} = \begin{bmatrix} \triangle\phi_r \\ \triangle\theta_r \end{bmatrix}. \tag{33}$$

Solving (30) for the incremental tilting commands vector $\boldsymbol{\delta}$ yields

$$\boldsymbol{\delta} = \boldsymbol{M}^{-1}\left(\begin{bmatrix} \ddot{x}_{\text{ed}} \\ \ddot{y}_{\text{ed}} \end{bmatrix} - \boldsymbol{N}\right) \tag{34}$$

$$= -\frac{m}{T}\frac{1}{c_\phi^2 c_\theta}\begin{bmatrix} s_\psi c_\theta c_\phi & -c_\psi c_\theta c_\phi \\ c_\psi c_\phi + s_\psi s_\theta s_\phi & s_\psi c_\phi - c_\psi s_\theta s_\phi \end{bmatrix} \left(\begin{bmatrix} \ddot{x}_{\text{ed}} \\ \ddot{y}_{\text{ed}} \end{bmatrix} + \frac{T}{m}\begin{bmatrix} s_\psi s_\phi + c_\psi s_\theta c_\phi \\ -c_\psi s_\phi + s_\psi s_\theta c_\phi \end{bmatrix}\right). \tag{35}$$

We now prescribe the following asymptotically stable virtual (desired) dynamics of the Quadrotor's center of gravity O_B in arbitrary horizontal inertial planes

$$\ddot{x}_e + c_1(\dot{x}_e - \dot{x}_{\text{ed}}) + c_2(x_e - x_{\text{ed}}) = \ddot{x}_{\text{ed}} \tag{36}$$

and

$$\ddot{y}_e + c_3(\dot{y}_e - \dot{y}_{\text{ed}}) + c_4(y_e - y_{\text{ed}}) = \ddot{y}_{\text{ed}} \tag{37}$$

where c_1, c_2, c_3, and c_4 are strictly positive scalars that are chosen to obtain any desired damping ratios and natural frequencies of the two second-order dynamics. The reference incremental variables $\triangle\phi_r$ and $\triangle\theta_r$ are obtained by substituting $\ddot{x}_{\text{ed}}$ and $\ddot{y}_{\text{ed}}$ from (36) and (37) into (35). Finally, the expressions for ϕ_r and θ_r are obtained as $\phi_r = \phi(t) + \triangle\phi$ and $\theta_r = \theta(t) + \triangle\theta$.

The outer loop also generates the thrust variable T that controls the inertial altitude variable z_e. Solving the third scalar equation of (13) for T yields

$$T = \frac{m}{c_\theta c_\phi}(g - \ddot{z}_e). \tag{38}$$

Hence, we prescribe the following asymptotically stable virtual altitude dynamics of O_B

$$(\ddot{z}_e - \ddot{z}_{\text{ed}}) + c_5(\dot{z}_e - \dot{z}_{\text{ed}}) + c_6(z_e - z_{\text{ed}}) = 0 \tag{39}$$

where c_5 and c_6 are strictly positive scalars. The thrust variable T is obtained by solving (39) for $\ddot{z}_e$ and substituting in (38), resulting in

$$T = \frac{m}{c_\theta c_\phi}[g - \ddot{z}_{\text{ed}} + c_5(\dot{z}_e - \dot{z}_{\text{ed}}) + c_6(z_e - z_{\text{ed}})]. \tag{40}$$

5 Inner RGDI control loop design

The aim from the inner RGDI control loop is to determine the three control torques that are required to track the reference roll tilting command ϕ_r, the reference pitch tilting command θ_r, and the desired yaw attitude command ψ_{d} that are generated by the outer loop. The particular and the auxiliary parts of the RGDI control law are designed in this paper to control the tilting and attitude angles and to stabilize the Quadrotor's body angular velocity components, respectively. Hence, we define the following outer and inner angular state vectors

$$\boldsymbol{x}_o = \begin{bmatrix} \phi & \theta & \psi \end{bmatrix}^{\text{T}} \tag{41}$$

$$\boldsymbol{x}_i = \begin{bmatrix} p & q & r \end{bmatrix}^{\text{T}}. \tag{42}$$

The outer and the inner attitude dynamics given by (17) and (22) are rewritten accordingly in the following compact forms

$$\dot{\boldsymbol{x}}_o = \boldsymbol{\Gamma}(\phi, \theta)\boldsymbol{x}_i \tag{43}$$

and

$$\dot{\boldsymbol{x}}_i = \boldsymbol{A}_i + \boldsymbol{J}^{-1}\boldsymbol{\tau} \tag{44}$$

where

$$\boldsymbol{A}_i = \boldsymbol{J}^{-1}\begin{bmatrix} qr(J_y - J_z) \\ pr(J_z - J_x) \\ pq(J_x - J_y) \end{bmatrix} + J_r\boldsymbol{J}^{-1}\begin{bmatrix} -q\sum_{i=1}^{4}\omega_i \\ p\sum_{i=1}^{4}\omega_i \\ -\sum_{i=1}^{4}\dot{\omega}_i \end{bmatrix}. \tag{45}$$

We also define the following desired outer and inner state vectors

$$\boldsymbol{x}_{od} = \begin{bmatrix}\phi_r & \theta_r & \psi_{\mathrm{d}}\end{bmatrix}^{\mathrm{T}} \tag{46}$$

$$\boldsymbol{x}_{id} = \begin{bmatrix}p_d & q_d & r_d\end{bmatrix}^{\mathrm{T}}. \tag{47}$$

5.1 GDI baseline control law design

The outer state error vector $\boldsymbol{e}_o = \begin{bmatrix}e_\phi & e_\theta & e_\psi\end{bmatrix}^{\mathrm{T}}$ is defined as

$$\boldsymbol{e}_o = \boldsymbol{x}_o - \boldsymbol{x}_{od}(t) \tag{48}$$

$$= \begin{bmatrix}\phi - \phi_r(t) & \theta - \theta_r(t) & \psi - \psi_{\mathrm{d}}(t)\end{bmatrix}^{\mathrm{T}}. \tag{49}$$

Also, the angular state deviation function is defined as

$$\chi = k_1(\phi - \phi_r)^2 + k_2(\theta - \theta_r)^2 + k_3(\psi - \psi_d)^2 = \boldsymbol{e}_o^T\,\mathrm{diag}(k_1, k_2, k_3)\boldsymbol{e}_o \tag{50}$$

where $k_j,\ j = 1, 2, 3$ are strictly positive constants, and $\mathrm{diag}(k_1, k_2, k_3)$ is the 3×3 diagonal matrix containing k_1, k_2, and k_3 in its diagonal entries. A linear ordinary differential constraint equation is now formulated in χ, the differential order of which is the same as the relative degree of the deviation function. The equation takes the form

$$\ddot{\chi} + a_1\dot{\chi} + a_2\chi = 0 \tag{51}$$

where a_1 and a_2 are chosen such that the constraint dynamics is asymptotically stable. The two time derivatives of χ are evaluated as:

$$\dot{\chi} = 2\boldsymbol{e}_o^T\,\mathrm{diag}(k_1, k_2, k_3)\dot{\boldsymbol{e}}_o \tag{52}$$

and

$$\ddot{\chi} = 2\boldsymbol{e}_o^T\,\mathrm{diag}(k_1, k_2, k_3)[\boldsymbol{F} + \boldsymbol{G}\boldsymbol{\tau} - \ddot{\boldsymbol{x}}_{od}] + 2\dot{\boldsymbol{e}}_o^T\,\mathrm{diag}(k_1, k_2, k_3)\dot{\boldsymbol{e}}_o. \tag{53}$$

By substituting the expressions of χ and its first two time derivatives in (51), the differential form of constraint is converted to the following algebraic form

$$\mathcal{A}(\boldsymbol{x}_o, t)\boldsymbol{\tau} = B(\boldsymbol{x}_o, \boldsymbol{x}_i, t) \tag{54}$$

where

$$\mathcal{A}(\boldsymbol{x}_o, t) = 2\boldsymbol{e}_o^T\,\mathrm{diag}(k_1, k_2, k_3)\boldsymbol{G} \tag{55}$$

and

$$\begin{aligned} B(\boldsymbol{x}_o, \boldsymbol{x}_i, t) = &-2\dot{\boldsymbol{e}}_o^T\,\mathrm{diag}(k_1, k_2, k_3)\dot{\boldsymbol{e}}_o \\ &- 2a_1\boldsymbol{e}_o^T\,\mathrm{diag}(k_1, k_2, k_3)\dot{\boldsymbol{e}}_o \\ &- a_2\boldsymbol{e}_o^T\,\mathrm{diag}(k_1, k_2, k_3)\boldsymbol{e}_o \\ &- 2\boldsymbol{e}_o^T\,\mathrm{diag}(k_1, k_2, k_3)\boldsymbol{F} \\ &+ 2\boldsymbol{e}_o^T\,\mathrm{diag}(k_1, k_2, k_3)\ddot{\boldsymbol{x}}_{od}. \end{aligned} \tag{56}$$

The algebraic equation (54) is under-determined and consistent for all $(\boldsymbol{e}_o, \dot{\boldsymbol{e}}_o) \neq (\mathbf{o}_3, \mathbf{o}_3)$. Therefore, it has infinite number of solutions, and these solutions are parameterizable by the generalized inversion-based Greville formula as [45]

$$\boldsymbol{\tau} = \mathcal{A}^{+}(\boldsymbol{x}_o, t)B(\boldsymbol{x}_o, \boldsymbol{x}_i, t) + \boldsymbol{P}(\boldsymbol{x}_o, t)\boldsymbol{\zeta} \tag{57}$$

where $\mathcal{A}^{+}$ is the MPGI of $\mathcal{A}$, and it is given by

$$\mathcal{A}^{+}(\boldsymbol{x}_o, t) = \mathcal{A}^{T}(\boldsymbol{x}_o, t)\{\mathcal{A}(\boldsymbol{x}_o, t)\mathcal{A}^{T}(\boldsymbol{x}_o, t)\}^{-1} \tag{58}$$

and $\boldsymbol{P}$ is the projection matrix on the null space of $\mathcal{A}$, and is given by

$$\boldsymbol{P}(\boldsymbol{x}_o, t) = \boldsymbol{I}_{3\times 3} - \mathcal{A}^{+}(\boldsymbol{x}_o, t)\mathcal{A}(\boldsymbol{x}_o, t) \tag{59}$$

and $\boldsymbol{\zeta} \in \mathbb{R}^3$ is the null control vector, which is arbitrary for the purpose of enforcing the constraint dynamics given by (54), and it is designed in this paper to stabilize the Quadrotor's inner attitude dynamics. The inner state vector $\boldsymbol{e}_i = \begin{bmatrix}e_p & e_q & e_r\end{bmatrix}^{\mathrm{T}}$ is defined as

$$\boldsymbol{e}_i = \boldsymbol{x}_i - \boldsymbol{x}_{id}(t) = \begin{bmatrix}p - p_d(t) & q - q_d(t) & r - r_d(t)\end{bmatrix}^{\mathrm{T}}. \tag{60}$$

Then the GDI control law is [52]

$$\boldsymbol{\tau}^* = \mathcal{A}^*(\boldsymbol{x}_o, \nu, t)B(\boldsymbol{x}_o, \boldsymbol{x}_i, t) + \boldsymbol{P}(\boldsymbol{x}_o, t)\boldsymbol{\zeta} \tag{61}$$

where the dynamically scaled MPGI is given by

$$\mathcal{A}^*(\boldsymbol{x}_o, \nu, t) = \mathcal{A}^T(\boldsymbol{x}_o, t) \{\mathcal{A}(\boldsymbol{x}_o, t)\mathcal{A}^T(\boldsymbol{x}_o, t) + \nu(t)\}^{-1} \tag{62}$$

such that ν satisfies the first-order forced dynamics

$$\dot{\nu}(t) = -\nu(t) + \gamma \frac{\|\boldsymbol{e}_i(t)\|^2}{\|\boldsymbol{e}_o(t)\|^2}, \quad \gamma > 0, \quad \nu(0) > 0 \tag{63}$$

and $\|\cdot\|$ denotes the Euclidean norm.

5.2 Null control vector design

The aim from designing the null control vector $\boldsymbol{\zeta}$ is to stabilize the Quadrotor's inner (angular velocity) dynamics given by (44). Substituting the GDI control law $\boldsymbol{\tau}^\star$ given by (61) in (44) yields the following closed loop inner state dynamics

$$\dot{\boldsymbol{x}}_i = \boldsymbol{A}_i + \boldsymbol{J}^{-1}\{\mathcal{A}^\star(\boldsymbol{x}_o, \nu, t)B(\boldsymbol{x}_o, \boldsymbol{x}_i, t) + \boldsymbol{P}(\boldsymbol{x}_o, t)\boldsymbol{\zeta}\}. \tag{64}$$

The desired inner state dynamics is constructed as:

$$\dot{\boldsymbol{x}}_{id} = \boldsymbol{A}_{id} + \boldsymbol{J}^{-1}\{\mathcal{A}^\star(\boldsymbol{x}_o, \nu, t)B(\boldsymbol{x}_o, \boldsymbol{x}_{id}, t)\}. \tag{65}$$

where $\boldsymbol{A}_{id}$ is obtained by replacing p, q, and r in the expression of $\boldsymbol{A}_i$ given by (45) by p_d, q_d, and r_d. The inner state error dynamics is obtained by subtracting (65) from (64), resulting in

$$\dot{\boldsymbol{e}}_i = \triangle + \boldsymbol{J}^{-1}\boldsymbol{P}(\boldsymbol{x}_o, t)\boldsymbol{\zeta} \tag{66}$$

where

$$\triangle = \boldsymbol{A}_i - \boldsymbol{A}_{id} + \boldsymbol{J}^{-1}\mathcal{A}^\star(\boldsymbol{x}_o, \nu, t)\{B(\boldsymbol{x}_o, \boldsymbol{x}_i, t) - B(\boldsymbol{x}_o, \boldsymbol{x}_{id}, t)\}. \tag{67}$$

Consider the following radially unbounded positive definite control Lyapunov function

$$V(\boldsymbol{x}_o, \boldsymbol{x}_i, t) = \boldsymbol{e}_i^T \bar{\boldsymbol{P}}(\boldsymbol{x}_o, t)\boldsymbol{e}_i \tag{68}$$

where

$$\bar{\boldsymbol{P}}(\boldsymbol{x}_o, t) = \boldsymbol{I}_{3\times 3} - \delta\mathcal{A}^+\mathcal{A} \tag{69}$$

for a positive real scalar δ such that $|\delta| < 1$. The time derivative of V along the trajectories of inner error dynamical system given by (67) is

$$\dot{V} = 2\boldsymbol{e}_i^T \bar{\boldsymbol{P}}(\triangle + \boldsymbol{J}^{-1}\boldsymbol{P}\boldsymbol{\zeta}) + \boldsymbol{e}_i^T \dot{\bar{\boldsymbol{P}}}\boldsymbol{e}_i = \boldsymbol{e}_i^T(2\bar{\boldsymbol{P}}\triangle + 2\bar{\boldsymbol{P}}\boldsymbol{J}^{-1}\boldsymbol{P}\boldsymbol{\zeta} + \dot{\bar{\boldsymbol{P}}}\boldsymbol{e}_i) \tag{70}$$

where $\dot{\bar{\boldsymbol{P}}}$ is the element-wise time derivative of $\bar{\boldsymbol{P}}$ along the trajectories of $\dot{\boldsymbol{e}}_o$. Global asymptotic stability of inner dynamics is guaranteed by the existence of a symmetric positive definite matrix $\boldsymbol{Q}$ such that

$$\dot{V} = -{\boldsymbol{e}_i}^T\boldsymbol{Q}\boldsymbol{e}_i < 0. \tag{71}$$

Equating (70) and (71) yields

$$\boldsymbol{e}_i^T(2\bar{\boldsymbol{P}}\triangle + 2\bar{\boldsymbol{P}}\boldsymbol{J}^{-1}\boldsymbol{P}\boldsymbol{\zeta} + \dot{\boldsymbol{P}}\boldsymbol{e}_i + \boldsymbol{Q}\boldsymbol{e}_i) = 0 \tag{72}$$

for all $\boldsymbol{e}_i \neq \boldsymbol{o}_3$. Therefore, a sufficient condition for global asymptotic stability of $\boldsymbol{e}_i = \boldsymbol{o}_3$ is

$$2\bar{\boldsymbol{P}}\triangle + 2\bar{\boldsymbol{P}}\boldsymbol{J}^{-1}\boldsymbol{P}\boldsymbol{\zeta} + \dot{\boldsymbol{P}}\boldsymbol{e}_i + \boldsymbol{Q}\boldsymbol{e}_i = 0. \tag{73}$$

Solving for the projected null control vector $\boldsymbol{P}\boldsymbol{\zeta}$ yields

$$\boldsymbol{P}\boldsymbol{\zeta} = -(\bar{\boldsymbol{P}}\boldsymbol{J}^{-1})^{-1}\boldsymbol{P}\left(\bar{\boldsymbol{P}}\triangle + \frac{\dot{\boldsymbol{P}}}{2}\boldsymbol{e}_i + \frac{\boldsymbol{Q}}{2}\boldsymbol{e}_i\right). \tag{74}$$

Therefore, the closed loop inner state dynamics given by (64) becomes

$$\dot{\boldsymbol{x}}_i = \boldsymbol{A}_i + \boldsymbol{J}^{-1}\mathcal{A}^\star(\boldsymbol{x}_o, \nu, t)B(\boldsymbol{x}_o, \boldsymbol{x}_i, t) - \boldsymbol{J}^{-1}(\bar{\boldsymbol{P}}\boldsymbol{J}^{-1})^{-1}\boldsymbol{P}\left(\bar{\boldsymbol{P}}\triangle + \frac{\dot{\boldsymbol{P}}}{2}\boldsymbol{e}_i + \frac{\boldsymbol{Q}}{2}\boldsymbol{e}_i\right) \tag{75}$$

and the resulting Quadrotor's dynamics is globally partially asymptotically stable with respect to the equilibrium inner error state $\boldsymbol{e}_i = \boldsymbol{o}_3$.

5.3 Integration of the RGDI robustness control term

In order to robustify the GDI control system performance against modeling uncertainties and external disturbances, an additional sliding mode robustness control term is augmented with the baseline GDI control law given by (61). The RGDI control law takes the following form

$$\boldsymbol{\tau}_a = \mathcal{A}^*(\boldsymbol{x}_o, \nu, t)B(\boldsymbol{x}_o, \boldsymbol{x}_i, t) + \boldsymbol{P}(\boldsymbol{x}_o, t)\boldsymbol{\zeta} - C\mathcal{A}^\star(\boldsymbol{x}_o, \nu, t)\frac{s}{|s|} \tag{76}$$

where C is a positive constant gain that enforces sliding, and s is the sliding surface defined as

$$s = \dot{\chi} + a_1\chi + a_2\int \chi \mathrm{d}t. \tag{77}$$

The time derivative of s is

$$\dot{s} = \ddot{\chi} + a_1\dot{\chi} + a_2\chi. \tag{78}$$

Notice that asymptotic (or finite time) convergence of $\dot{s}$ to zero implies asymptotic (or finite time) realization of the differential constraint dynamics given by (51) and its algebraic equivalence given by (54). Equation (78) can be written in terms of $\mathcal{A}(\boldsymbol{x}_o, t)$ and $B(\boldsymbol{x}_o, \boldsymbol{x}_i, t)$ as

$$\dot{s} = \mathcal{A}(\boldsymbol{x}_o, t)\boldsymbol{\tau} - B(\boldsymbol{x}_o, \boldsymbol{x}_i, t) \tag{79}$$

where $\dot{s} = 0$ if $\boldsymbol{\tau}$ is given by (57). Instead, if the expression of $\boldsymbol{\tau}_a$ that is given by (76) is substituted in (79) then

$$\begin{aligned}
\dot{s} &= \mathcal{A}(\boldsymbol{x}_o, t)\left\{\mathcal{A}^*(\boldsymbol{x}_o, \nu, t)B(\boldsymbol{x}_o, \boldsymbol{x}_i, t) + \boldsymbol{P}(\boldsymbol{x}_o, t)\boldsymbol{\zeta} - C\mathcal{A}^\star(\boldsymbol{x}_o, \nu, t)\frac{s}{|s|}\right\} - B(\boldsymbol{x}_o, \boldsymbol{x}_i, t) \\
&= \mathcal{A}(\boldsymbol{x}_o, t)\left\{\mathcal{A}^*(\boldsymbol{x}_o, \nu, t)B(\boldsymbol{x}_o, \boldsymbol{x}_i, t) + \left[\boldsymbol{I}_{3\times 3} - \mathcal{A}^+(\boldsymbol{x}_o, t)\mathcal{A}(\boldsymbol{x}_o, t)\right]\boldsymbol{\zeta} - C\mathcal{A}^*(\boldsymbol{x}_o, \nu, t)\frac{s}{|s|}\right\} - B(\boldsymbol{x}_o, \boldsymbol{x}_i, t) \\
&= \mathcal{A}(\boldsymbol{x}_o, t)\mathcal{A}^*(\boldsymbol{x}_o, \nu, t)B(\boldsymbol{x}_o, \boldsymbol{x}_i, t) - C\mathcal{A}(\boldsymbol{x}_o, t)\mathcal{A}^*(\boldsymbol{x}_o, \nu, t)\frac{s}{|s|} - B(\boldsymbol{x}_o, \boldsymbol{x}_i, t)
\end{aligned} \tag{80}$$

where the following MPGI property is used [45]

$$\mathcal{A}(\boldsymbol{x}_o, t)\mathcal{A}^+(\boldsymbol{x}_o, t)\mathcal{A}(\boldsymbol{x}_o, t) = \mathcal{A}(\boldsymbol{x}_o, t). \tag{81}$$

Moreover, define $\delta_{\mathcal{A}}(\boldsymbol{x}_o, \nu, t)$ as

$$\delta_{\mathcal{A}}(\boldsymbol{x}_o, \nu, t) = \mathcal{A}(\boldsymbol{x}_o, t)\mathcal{A}^*(\boldsymbol{x}_o, \nu, t) \tag{82}$$

then the expression of $\dot{s}$ given by (80) reduces to

$$\dot{s} = \{\delta_{\mathcal{A}}(\boldsymbol{x}_o, \nu, t) - 1\}\mathcal{B}(\boldsymbol{x}_o, \boldsymbol{x}_i, t) - C\delta_{\mathcal{A}}(\boldsymbol{x}_o, \nu, t)\frac{s}{|s|}. \tag{83}$$

Because $\nu \in (0, \infty)$, the expression of $\mathcal{A}^*(\boldsymbol{x}_o, \nu, t)$ given by (62) implies that

$$0 < \delta_{\mathcal{A}}(\boldsymbol{x}_o, \nu, t) < 1 \tag{84}$$

for all $\mathcal{A}(\boldsymbol{x}_o, t) \neq \mathbf{o}_{1\times 3}$, and that

$$\lim_{t\to\infty} \delta_{\mathcal{A}}(\boldsymbol{x}_o, \nu, t) = 0 \;\Leftrightarrow\; \lim_{t\to\infty} \mathcal{A}(\boldsymbol{x}_o, t) = \mathbf{o}_{1\times 3}. \tag{85}$$

The following positive definite control Lyapunov function

$$V = \frac{1}{2}s^2 \tag{86}$$

is utilized now to design the sliding mode gain C. The time derivative of V along solution trajectories of the sliding variable dynamics given by (83) is

$$\dot{V} = s\dot{s} = s\{\delta_{\mathcal{A}}(\boldsymbol{x}_o, \nu, t) - 1\}\mathcal{B}(\boldsymbol{x}_o, \boldsymbol{x}_i, t) - C\delta_{\mathcal{A}}(\boldsymbol{x}_o, \nu, t)|s|. \tag{87}$$

Therefore, if the constant sliding mode gain, C is replaced by the following function

$$C(\boldsymbol{x}_o, \boldsymbol{x}_i, \nu, t) = C_0 + \frac{1 - \delta_{\mathcal{A}}(\boldsymbol{x}_o, \nu, t)}{\delta_{\mathcal{A}}(\boldsymbol{x}_o, \nu, t)}|\mathcal{B}(\boldsymbol{x}_o, \boldsymbol{x}_i, t)| \tag{88}$$

where $C_0 > 0$, then $\dot{V}$ would be negative definite, and hence finite-time stability of $s = 0$ follows from Lyapunov's direct method [60] and the discontinuous sliding mode term in the expression of $\dot{s}$ given by (83). Moreover, this would also implies asymptotic stability of $\chi = 0$ and $\boldsymbol{e}_o = \mathbf{o}_{3\times 1}$ as evident from the dynamics of s given by (78). Nevertheless, this would also implies convergence of $\mathcal{A}(\boldsymbol{x}_o, t)$ to $\mathbf{o}_{1\times 3}$. Hence, it follows from (85) that $\delta_{\mathcal{A}}(\boldsymbol{x}_o, \nu, t)$ must also converge to zero. Therefore,

$$\lim_{\boldsymbol{e}_o\to\mathbf{o}_3} \frac{1 - \delta_{\mathcal{A}}(\boldsymbol{x}_o, \nu, t)}{\delta_{\mathcal{A}}(\boldsymbol{x}_o, \nu, t)} = \infty \tag{89}$$

which requires the function $C(\boldsymbol{x}_o, \boldsymbol{x}_i, \nu, t)$ to reach infinite values as $\boldsymbol{e}_o$ vanishes in order to guarantee negative definiteness of $\dot{V}$ and finite-time convergence of s to zero. Therefore, it is not feasible to design a SMC gain that guarantees finite time closed loop stability of the RGDI sliding mode dynamics given by (83).

However, the SMC gain can be designed to achieve semi-global practical stability of the sliding dynamics, as stated by the following proposition and theorem.

Proposition 1 *For every real number* $\delta^*_{\mathcal{A}} \in (0, 1)$ *there exists a real number* $C^* > 0$ *such that the time derivative of* V *along solution trajectories of the sliding mode dynamics given by* (83) *is strictly negative for all* $\delta_{\mathcal{A}}(\boldsymbol{x}_o, \nu, t) > \delta^*_{\mathcal{A}}$ *and for any constant gain* $C \geq C^*$.

Proof Let $\delta^*_{\mathcal{A}}$ be a prescribed real number in the range of $\delta_{\mathcal{A}}(\boldsymbol{x}_o, \nu, t)$, i.e., $\delta^*_{\mathcal{A}} \in (0, 1)$. Also, define $\bar{C}(\boldsymbol{x}_o, \boldsymbol{x}_i, t)$ as

$$\bar{C}(\boldsymbol{x}_o, \boldsymbol{x}_i, t) = C_0 + \frac{1 - \delta^*_{\mathcal{A}}}{\delta^*_{\mathcal{A}}} |\mathcal{B}(\boldsymbol{x}_o, \boldsymbol{x}_i, t)|. \tag{90}$$

It follows that if $\delta^*_{\mathcal{A}} < \delta_{\mathcal{A}}(\boldsymbol{x}_o, \nu, t)$ then $\bar{C}(\boldsymbol{x}_o, \boldsymbol{x}_i, t) > C(\boldsymbol{x}_o, \boldsymbol{x}_i, \nu, t)$. Accordingly, let $\mathcal{D}$ be a neighborhood of the point $\boldsymbol{e}_o = \mathbf{o}_3$, and choose a sliding mode gain constant C^* such that

$$C^* > \sup_{\mathcal{D},t} \bar{C}(\boldsymbol{x}_o, \boldsymbol{x}_i, t). \tag{91}$$

Then $\dot{V} < 0$ holds true along any closed loop trajectory that initiates within $\mathcal{D}$ whenever $\delta_{\mathcal{A}}(\boldsymbol{x}_o, \nu, t) > \delta^*_{\mathcal{A}}$ and for any constant gain $C \geq C^*$. The existence of a finite number C^* is guaranteed over any domain $\mathcal{D}$ because the baseline GDI control law given by (61) with the projected null control vector design given by (74) yield bounded $\boldsymbol{x}_o$ trajectories [52] and bounded $\boldsymbol{x}_i$ trajectories, respectively, which implies that $\mathcal{B}(\boldsymbol{x}_o, \boldsymbol{x}_i, t)$ is globally bounded. □

Theorem 1 *Consider the closed loop RGDI control system of the Quadrotor's model given by* (43) *and* (44)*, where the auxiliary part* $\boldsymbol{P\zeta}$ *of the RGDI control law* $\boldsymbol{\tau} = \boldsymbol{\tau}_a$ *given by* (76) *is given by* (74)*. If the sliding mode gain constant* C *is sufficiently big, then the closed loop system is partially semi-globally practically stable with respect to* $\boldsymbol{e}_o = \mathbf{o}_{3\times 1}$.

Proof It follows from Proposition 1 that $\delta^*_{\mathcal{A}}$ can be reduced arbitrarily close to zero by increasing the magnitude of the sliding mode gain C such that the condition $\dot{V} < 0$ holds over $\mathcal{D}$ except for a diminishing domain $\mathcal{D}_0 \subset \mathcal{D}$ that contains $\boldsymbol{x}_o = \boldsymbol{x}_{od}$ and satisfies the condition $\delta_{\mathcal{A}}(\boldsymbol{x}_o, \nu, t) < \delta^*_{\mathcal{A}}$ for all $\boldsymbol{x}_o \in \mathcal{D}_0$. Since the error state trajectory $\boldsymbol{e}_o$ must enter $\mathcal{D}_0$ in finite time and remain within that domain, it follows that driving $\delta^*_{\mathcal{A}}$ arbitrarily closer to zero implies driving $\boldsymbol{e}_o$ arbitrarily closer to $\mathbf{o}_3$ and making $\mathcal{D}_0$ invariant, i.e., making $\boldsymbol{e}_o$ uniformly ultimately bounded and making $\boldsymbol{e}_o = \mathbf{o}_{3\times 1}$ practically stable. Moreover, because $\mathcal{D}$ can be arbitrarily enlarged by increasing the magnitude of C, and since the $\boldsymbol{e}_i$ trajectories are globally bounded by virtue of implementing the $\boldsymbol{P\zeta}$ design given by (74), then the practical stability of $\boldsymbol{e}_o = \mathbf{o}_3$ is semi-global. □

Remark 1 The robustifying SMC design becomes independent from the null control vector $\boldsymbol{\zeta}$ as a consequence of eliminating $\boldsymbol{\zeta}$ from (80). For that reason, the SMC element preserves the geometric structure of the baseline GDI control law given by (61). Actually, the RGDI control law given by (76) can be rewritten as

$$\boldsymbol{\tau}_a = \overbrace{\mathcal{A}^*(\boldsymbol{x}_o, \nu, t) \left\{ \mathcal{B}(\boldsymbol{x}_o, \boldsymbol{x}_i, t) - C \frac{s}{|s|} \right\}}^{\in \mathcal{R}(\mathcal{A}^T)} + \underbrace{\boldsymbol{P}(\boldsymbol{x}_o, t)\boldsymbol{\zeta}}_{\in \mathcal{N}(\mathcal{A})} \tag{92}$$

which consists of two parts that act on two orthogonally complement subspaces of the control space: a particular part that acts on the range space $\mathcal{R}(\mathcal{A}^T)$ and an auxiliary part that acts on the null space $\mathcal{N}(\mathcal{A})$. This mutual orthogonality of the two control subspaces allows to design the particular control law independently from the auxiliary control law.

6 Numerical simulations and experimental results

To assess the performance of the RGDI control system, both numerical simulations and experimental tests are conducted. The numerical simulations are performed on a six DoFs mathematical model of the Quanser's 3 DoF Hover system shown in Fig. 3. Apart from numerical simulations, lab experiments are also performed on the 3 DoF Hover system experimental setup to visualize real-time performance of the inner RGDI (attitude) control loop. The inertia and aerodynamic parameters of the Quanser's 3 DoF Hover system are shown in Table 1.

6.1 Numerical simulations

The numerical simulations are performed under nominal and perturbed flight conditions to test the control

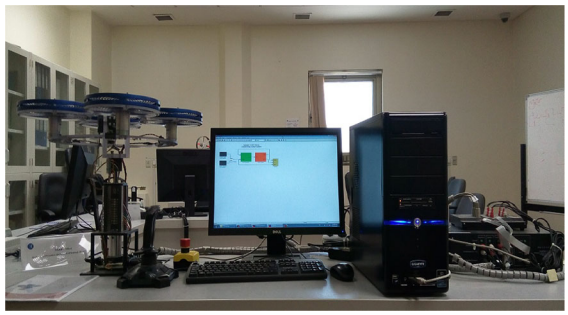

Fig. 3 Hardware setup of Quanser's 3 DoF Hover

Table 1 Quanser's 3 DoF Hover specifications

Parameters	Description	Value	Unit
m	Mass	2.850	kg
d	Arm length	0.280	m
I_x	Inertia	0.055	$\mathrm{kg\,m^2}$
I_y	Inertia	0.055	$\mathrm{kg\,m^2}$
I_z	Inertia	0.110	$\mathrm{kg\,m^2}$
b	Thrust factor	$0.877\mathrm{e}^{-5}$	–
k	Drag factor	$1.527\mathrm{e}^{-4}$	–

system performance against parametric uncertainties and external disturbances. The control system parameters are chosen to be $a_1 = 500$, $a_2 = 2000$, $k_1 = k_2 = 2$, $k_3 = 1$, and $C = 3.0$. The following two maneuvering scenarios are considered for computer simulations:

6.1.1 Waypoints following: nominal conditions

The Quadrotor in this scenario is commanded to follow a set of pre-defined waypoints as shown in Table 2 under nominal flight conditions. The three-dimensional plot shown in Fig. 4 depicts the Quadrotor's waypoint following performance. The roll, pitch, and yaw attitude profiles are shown in Fig. 5. The time histories of the control input commands T, τ_x, τ_y and τ_z are illustrated in Fig. 6, demonstrating that the control input requirement is so much realizable.

6.1.2 Helical trajectory tracking: perturbed conditions

In this scenario, the Quadrotor's desired trajectories are chosen as $x_{\mathrm{ed}} = 10\sin 2\pi t\,m$, $y_{\mathrm{ed}} = 10\cos 2\pi t\,m$, and $z_{\mathrm{ed}} = -t\,m$, such that a helical flight trajectory

Table 2 Waypoints

Waypoint	x_e (m)	y_e (m)	$-z_e$ (m)
1	0	0	0
2	0	0	6
3	15	0	12
4	15	15	18
5	−15	15	24
6	−15	−15	30
7	15	−15	36
8	15	15	48
9	−15	15	63
10	−15	0	72
11	−15	−15	90

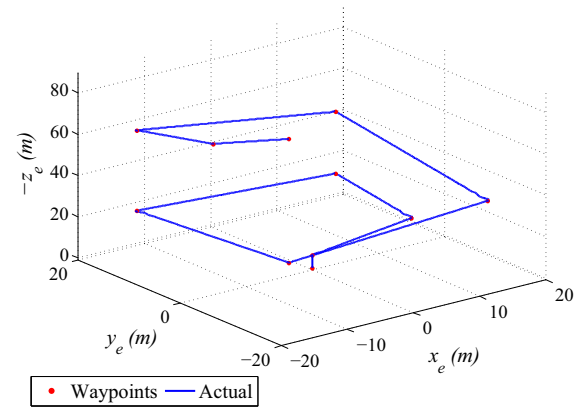

Fig. 4 Waypoints following in 3D: Nominal conditions

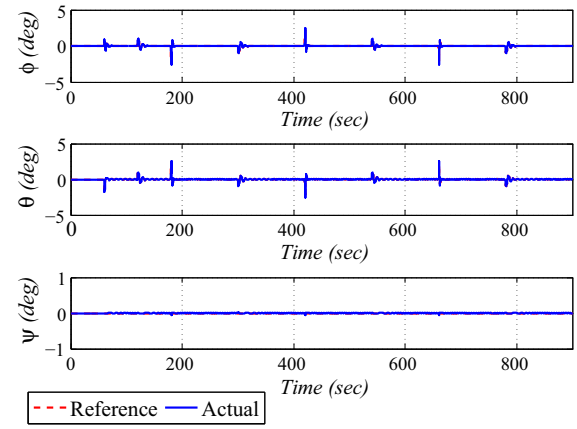

Fig. 5 Waypoints following: Tilting/attitude versus time: Nominal conditions

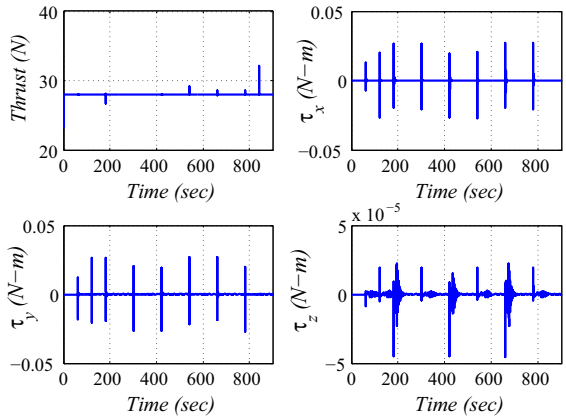

Fig. 6 Waypoints following: Control inputs versus time: Nominal conditions

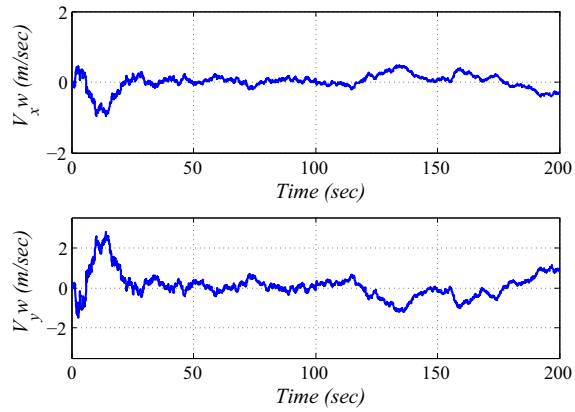

Fig. 7 Wind velocity versus time

is generated. To assess robustness, random parametric variations of $\pm 20\%$ in the numerical values of some Quadrotor's parameters are included in the mathematical model, such as mass, moments of inertia, aerodynamic thrust and drag coefficients, and the distance between propeller plane and center of gravity (arm length). External disturbances effects are also considered by simulating wind profiles that are generated by using the Dryden model, the wind velocity components of which are shown in Fig. 7. The tracking performance in the three-dimensional space subjected to wind disturbance and parametric variations is shown in Fig. 8. The trajectory tracking performance along the x_e, y_e, and z_e axes are depicted in Fig. 9. The tilting and attitude angles responses are shown in Fig. 10, and the time histories of the thrust force and the control torques are shown in Fig. 11. The simulations results demonstrate that the proposed RGDI control system is efficient and robust in the face of parametric uncertainties and exogenous disturbances.

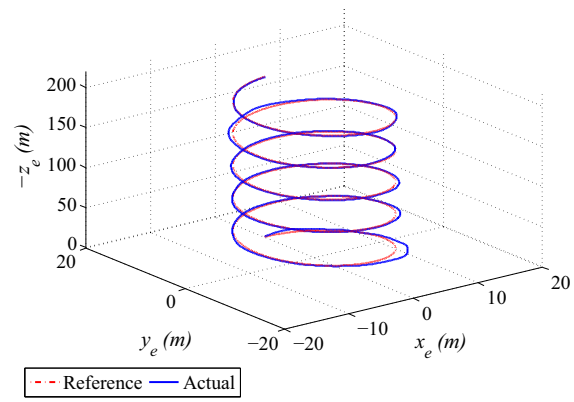

Fig. 8 Position tracking in 3D: Perturbed conditions

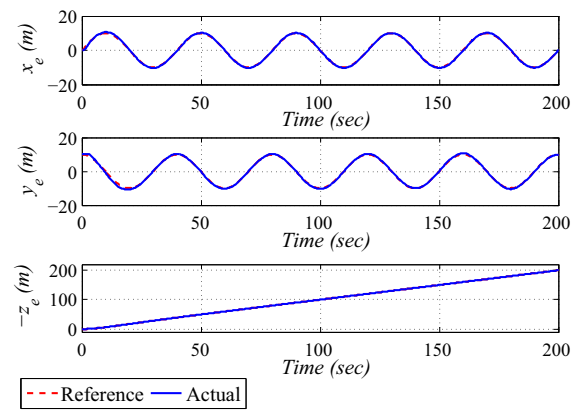

Fig. 9 Positional coordinates versus time: Perturbed conditions

6.2 Experimental tests on Quanser's 3 DoF Hover system

This section presents the experimental results that are obtained by implementing the RGDI control system for attitude control of the Quanser's 3 DoF Hover experimental setup. The system consists of a frame with four propellers. The frame is mounted on a three DoF pivot joint that enables the body to rotate about the roll, the pitch, and the yaw axes. The following hardware and software are also used:

- Power Module (Quanser VoltPAQ)
- Data Acquisition Board (Quanser Q8-USB, QPID/QPIDe)

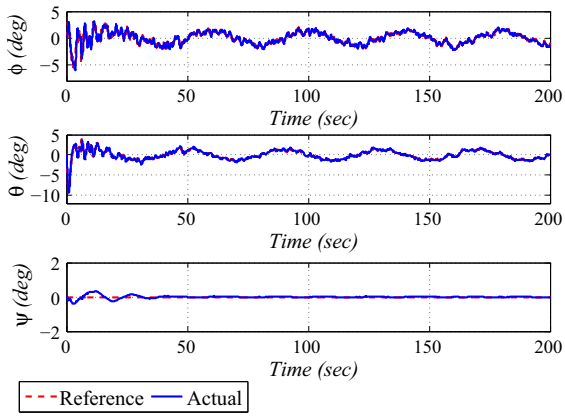

Fig. 10 Tiltling/attitude angles versus time: Perturbed conditions

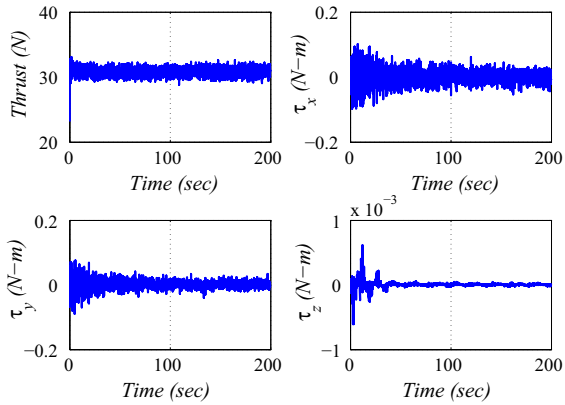

Fig. 11 Control inputs versus time: Perturbed conditions

– Hover Speciality Plant (Quanser hover)
– Real-Time Control Software (The QUARC-Simulink configuration).

The experimental control system parameters are chosen to be $a_1 = 2200$, $a_2 = 18{,}000$, $k_1 = k_2 = 12$, $k_3 = 2$, and $C = 0.5$. The experimental results are presented for the following maneuvering scenarios:

6.2.1 Sinusoidal tracking

Sinusoidal attitude profiles having amplitudes of ±5 deg with 0.1 Hz frequency are commanded in this scenario to the pitch and roll channels. The yaw channel is commanded to follow zero attitude. The experimental attitude tracking performance is shown in Fig. 12, and the corresponding control torques are shown in Fig. 13.

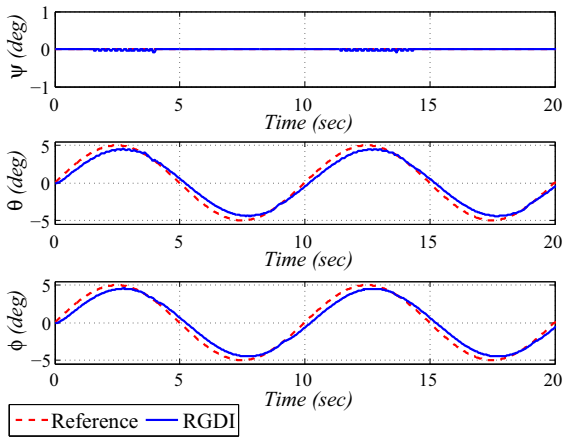

Fig. 12 Experimental results: Attitude angles versus time

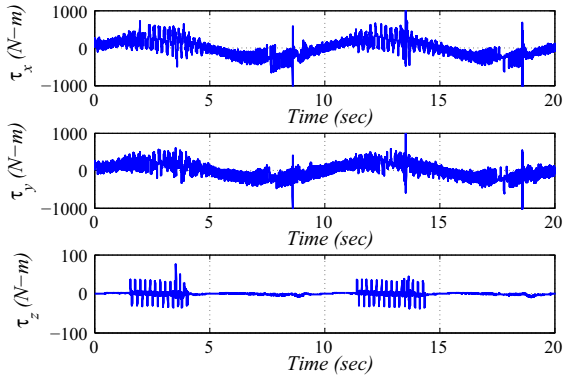

Fig. 13 Experimental results: Control torques versus time

6.2.2 Experimental comparisons: RGDI versus LQR and SMC

Comparative experimental tests were performed by implementing RGDI, LQR, and SMC control strategies on the Quanser 3 DoF Hover system. Two square waveform profiles, each having an amplitude of ±1 deg with a frequency of 0.05 Hz were commanded as reference inputs to the pitch and the roll channels, while the yaw attitude profile was commanded to maintain the zero angle. It is evident from Figs. 14, 15 and 16 that all the three control strategies yield successful following of the square waveform profiles. Nevertheless, RGDI and SMC control demonstrate a better tracking performance as compared to the classical LQR technique. The tracking response of RGDI in terms of the rise time is bit faster then SMC control, whereas a minor difference in steady-state error is also observed, which

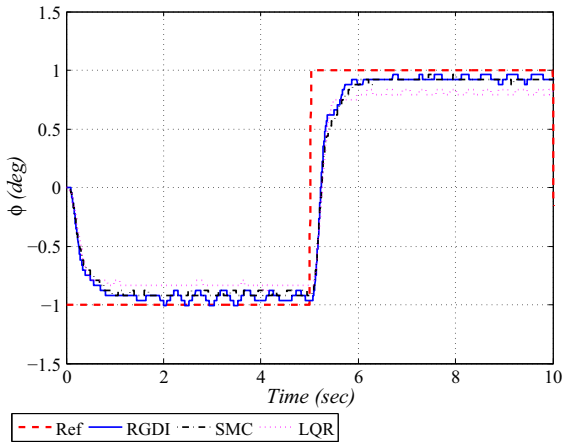

Fig. 14 Comparison (square-wave): Roll angle versus time

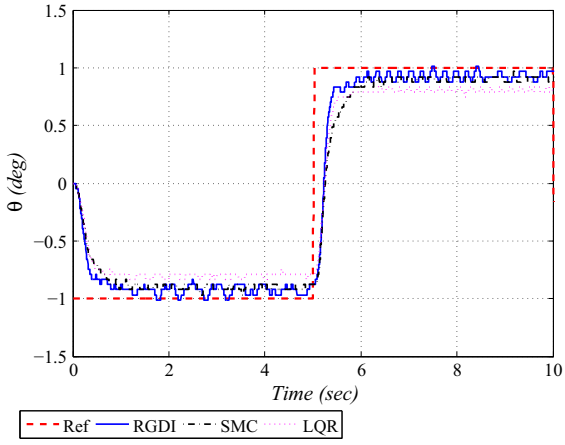

Fig. 15 Comparison (square-wave): Pitch angle versus time

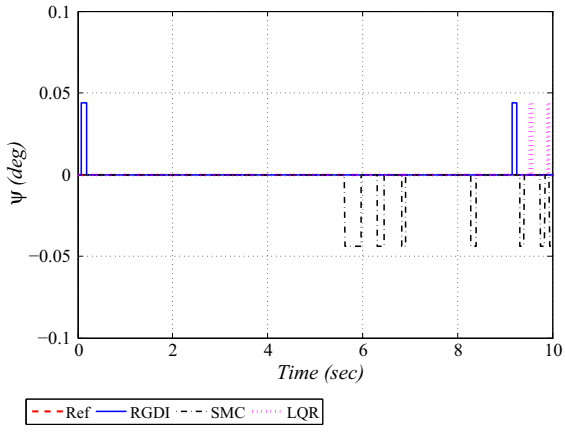

Fig. 16 Comparison (square-wave): Yaw angle versus time

is visualized by the squared error norm plot as shown in Fig. 17. The corresponding control torques generated by the three control strategies are depicted in Fig. 18.

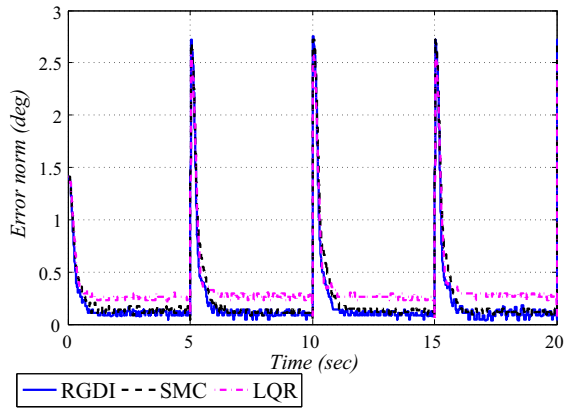

Fig. 17 Comparison (square-wave): Norm of errors versus time

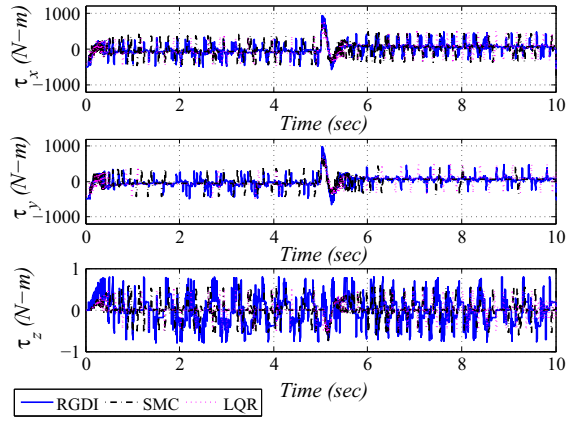

Fig. 18 Comparison (square-wave): Control torques versus time

Further comparative experimental tests were also performed by implementing RGDI, SMC and LQR control methodologies on the 3 DoF Hover system to generate random attitude profiles. The random attitude profiles were commanded to the pitch and the roll channels by using the analog joystick (Logitech Attack 3 USB) that is supplied with the Hover system. The tracking performance by employing all the three control strategies is shown in Fig. 19, which demonstrate that the RGDI control exhibits better and accurate tracking performance, as compared to classical LQR and conventional SMC techniques. To have an insight of the magnitude of the residual attitude tracking error, the respective squared error norms are shown in Fig. 20. The maximum value of the residual error is 1.73°, 2.29° and 2.95°, respectively, for the RGDI, SMC and LQR control methods. The corresponding control torques are shown in Fig. 21, which are very much realizable. The

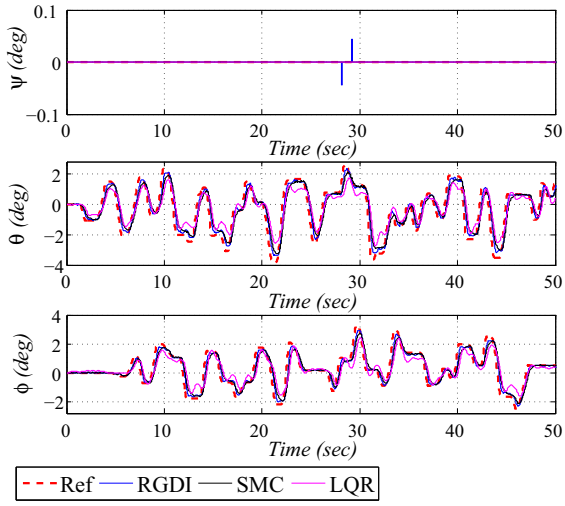

Fig. 19 Comparison (random profile): Attitude versus time

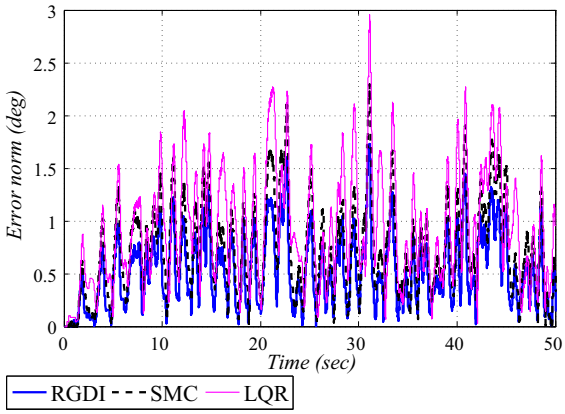

Fig. 20 Comparison (random profile): Norm of errors versus time

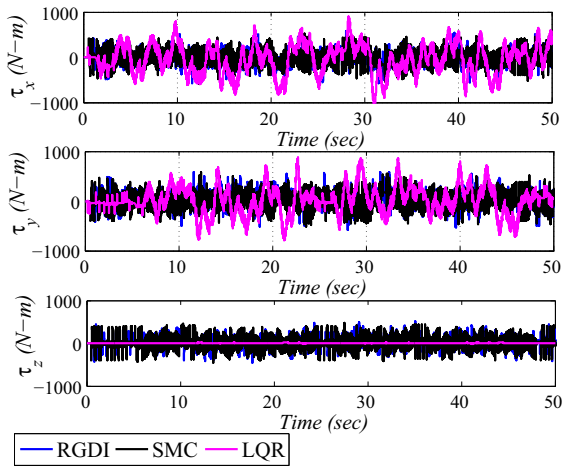

Fig. 21 Comparison (random profile): Control torques versus time

experimental analysis reveals that the proposed RGDI control system is competent enough for its real-time application to the complex nonlinear systems.

7 Conclusions

A two-loops structured control system is designed for Quadrotor's attitude and position control. The outer (slow) PD loop is based on linearizing the horizontal translational dynamics of the Quadrotor via the small disturbance theory, and it controls the three positional coordinates of the Quadrotor's CG by generating reference pitch and roll angles and generating the thrust command. The inner (fast) loop is based on RGDI control, and it controls the tilting and attitude angles by generating the control torque commands. The particular part of the RGDI control loop is augmented with a SMC element to enhance performance robustness against system's uncertainties and exogenous disturbances, guaranteeing finite-time semi-global practically stable attitude tracking. Numerical simulations are performed on a six DoF dynamic model of the Quadrotor, demonstrating robustness of the proposed RGDI controller under parametric uncertainties and wind disturbances. Experimental tests are also performed on the three DoF "Quanser's 3 DoF Hover" test bench. A comparative test of attitude control using RGDI, LQR and SMC methodologies is presented, showing the efficacy of the RGDI control design.

Compliance with ethical standards

Conflict of interest The authors certify that they have NO affiliation with or involvement in any organization or entity with any financial interest, or non-financial interest in the subject matter or materials discussed in this manuscript.

References

1. Ghazbi, S.N., Aghli, Y., Alimohammadi, M., Akbari, A.A.: Quadrotors unmanned aerial vehicles: a review. Int. J. Smart Sens. Intell. Syst. **9**(1), 309–333 (2016)
2. Mahony, R., Kumar, V., Corke, P.: Multirotor aerial vehicles: modeling, estimation, and control of quadrotor. IEEE Robot. Autom. Mag. **19**(3), 20–32 (2012)

3. Wang, S., Yang, Y.: Quadrotor aircraft attitude estimation and control based on Kalman filter. In: 31st Chinese Control Conference, Hefei, China, pp. 5634–5639 (2012)
4. Friedland, B.: Control System Design: An Introduction to State-Space Methods (Reprinted by Dover, 2005). McGrae-Hill Inc., New York (1986)
5. Ogata, K.: Modern Control Engineering, 4th edn. Pearson, London (2009)
6. Nise, N.S.: Control Systems Engineering, 7th edn. Wiley, Hoboken (2015)
7. Bouabdallah, S., Noth, A., Siegwart, R.: PID vs LQ control techniques applied to an indoor micro quadrotor. In: IEEE/RSJ International Conference on Intelligent Robots and Systems, Sendai, Japan, pp. 2451–2456 (2004)
8. Erginer, B., Altug, E.: Modeling and PD control of a Quadrotor VTOL vehicle. In: IEEE Intelligent Vehicles Symposium, Istanbul, Turkey, pp. 894–899 (2007)
9. Pounds, P., Mahony, R., Corke, P.: Modelling and control of a large quadrotor robot. Control Eng. Pract. **18**(7), 691–699 (2010)
10. Li, J., Li, Y.: Dynamic analysis and PID control for a quadrotor. In: International Conference on Mechatronics and Applications, Beijing, China, pp. 573–578 (2011)
11. ElKholy, Ht.M.: Dynamic modeling and control of a quadrotor using linear and nonlinear approaches. In: Masters Thesis, School of Science and Engineering, American University in Cairo, Cairo (2014)
12. Kokotovic, P.V.: The joy of feedback: nonlinear and adaptive. IEEE Control Syst. Mag. **12**(3), 7–17 (1992)
13. Lozano, R., Brogliato, B.: Adaptive control of robot manipulators with flexible joints. IEEE Trans. Autom. Control **37**(2), 174–181 (1992)
14. Zhou, J., Wen, C.: Adaptive Backstepping Control of Uncertain Systems: Nonsmooth Nonlinearities, Interactions or Time-Variations. Springer, New York (2008)
15. Mian, A.A., Daobo, W.: Modeling and backstepping-based nonlinear control strategy for a 6 DOF quadrotor helicopter. Chin. J. Aeronaut. **21**(3), 261–268 (2008)
16. Khalil, H.K.: Nonlinear Control. Pearson Education, London (2015)
17. Yang, Y., Yan, Y.: Attitude regulation for unmanned quadrotors using adaptive fuzzy gain-scheduling sliding mode control. Aerosp. Sci. Technol. **54**, 208–217 (2016)
18. Slotine, J.E., Li, W.: Applied Nonlinear Control. Pearson, London (1991)
19. Utkin, V., Guldner, J., Shi, J.: Sliding Mode Control in Electro-Mechanical Systems, 2nd edn. CRC Press, Boca Raton (2009)
20. Edwards, C., Spurgeon, S.: Sliding Mode Control: Theory and Applications. CRC Press, Boca Raton (1998)
21. Hamayun, M.T., Edwards, C., Alwi, H.: Fault Tolerant Control Schemes using Integral Sliding Modes. Springer, New York (2016)
22. Xu, R., Ozguner, U.: Sliding mode control of a quadrotor helicopter. In: IEEE Conference on Decision and Control, San Diego, CA, USA, pp. 4957–4962 (2006)
23. Bouadi, H., Cunha, S.S., Drouin, A., Camino, F.M.: Adaptive sliding mode control for quadrotor attitude stabilization and altitude tracking. In: International Symposium on Computational Intelligence and Informatics, Budapest, Hungary, pp. 449–455 (2011)
24. Runcharoon, K., Srichatrapimuk, V.: Sliding mode control of quadrotor. In: International Conference on Technological Advances in Electrical, Electronics and Computer Engineering, Konya, Turkey, pp. 552–557 (2013)
25. Arellano-Muro, C.A., Castillo-Toledo, B., Loukianov, A.G., Luque-Vega, L.F., González-Jiménez, L.E.: Quaternion-based trajectory tracking robust control for a quadrotor. In: System of Systems Engineering Conference, San Antonio, TX, USA, pp. 386–391 (2015)
26. Xiong, J.J., Zheng, E.H.: Position and attitude tracking control for a quadrotor UAV. ISA Trans. **53**(3), 725–731 (2014)
27. Zheng, E.H., Xiong, J.J., Luo, J.L.: Second order sliding mode control for a quadrotor UAV. ISA Trans. **53**(4), 1350–1356 (2014)
28. Xiong, J.J., Zhang, G.: Discrete-time sliding mode control for a quadrotor UAV. Opt. Int. J. Light Electron Opt. **127**(8), 3718–3722 (2016)
29. Xiong, J.J., Zhang, G.B.: Global fast dynamic terminal sliding mode control for a quadrotor UAV. ISA Trans. **66**, 233–240 (2017)
30. Ansari, U., Bajodah, A., Hamayun, M.T.: Quadrotor control via robust generalized dynamic inversion and adaptive nonsingular terminal sliding mode. Asian J. Control https://doi.org/10.1002/asjc.1800 (2018)
31. Das, A., Lewis, F.L., Subbarao, K.: Sliding Mode Approach to Control Quadrotor Using Dynamic Inversion. INTECH Open Access Publisher, Rijeka (2011)
32. Voos, H.: Nonlinear control of a quadrotor micro-UAV using feedback-linearization. In: IEEE International Conference on Mechatronics, Malaga, Spain, pp. 1–6 (2009)
33. Tiwari, S.N., Padhi, R.: Simultaneous attitude control and trajectory tracking of a micro quadrotor: a SNAC aided nonlinear dynamic inversion. In: American Control Conference, Washington, DC, USA, pp. 194–199 (2013)
34. Bloch, A.: Nonholonomic Mechanics and Control. Springer, New York (2003)
35. Bullo, F., Lewis, A.: Geometric Control of Mechanical Systems. Springer, New York (2005)
36. Lee, T., Leok, M., McClamroch, N.H.: Geometric tracking control of a quadrotor UAV on SE(3). In: Conference on Decision and Control, Atlanta, GA, USA, pp. 5420–5425 (2010)
37. Sreenath, K., Lee, T., Kumar, V.: Geometric control and differential flatness of a quadrotor UAV with a cable-suspended load. In: Conference on Decision and Control, Florence, Italy, pp. 2269–2274 (2013)
38. Lee, T.: Geometric control for a tethered quadrotor UAV. In: Conference on Decision and Control, Osaka, Japan, pp. 2749–2754 (2015)
39. Özbek, N.S., Önkol, M., Efe, M.O.: Feedback control strategies for quadrotor-type aerial robots: a survey. Trans. Inst. Meas. Control **38**(5), 529–554 (2016)
40. Bajodah, A.H., Hodges, D.H., Chen, Y.H.: Inverse dynamics of servo-constraints based on the generalized inverse. Nonlinear Dyn. **39**(1), 179–196 (2005)
41. Bajodah, A.H.: Singularly perturbed feedback linearization with linear attitude deviation dynamics realization. Nonlinear Dyn. **53**(4), 321–343 (2008)
42. Moore, E.H.: On the reciprocal of the general algebraic matrix. Bull. Am. Math. Soc. **26**, 394–395 (1920)

43. Penrose, R.: A generalized inverse for matrices. Proc. Camb. Philos. Soc. **51**, 406–413 (1955)
44. Greville, T.N.E.: The pseudoinverse of a rectangular or singular matrix and its applications to the solutions of systems of linear equations. SIAM Rev. **1**(1), 3843 (1959)
45. Ben-Israel, A., Greville, T.N.E.: Generalized Inverses: Theory and Applications, 2nd edn. Springer, New York (2003)
46. Udwadia, F.E., Kalaba, R.E.: Analytical Dynamics, A New Approach. Cambridge University Press, Cambridge (1996)
47. Enns, D., Bugajski, D., Hendrick, R., Stein, G.: Dynamic inversion: an evolving methodology for flight control design. Int. J. Control **59**(1), 71–91 (1994)
48. Pedro, J.O., Panday, A., Dala, L.: A nonlinear dynamic inversion-based neurocontroller for unmanned combat aerial vehicles during aerial refuelling. Int. J. Appl. Math. Comput. Sci. **23**(1), 75–90 (2013)
49. Ireland, M.L., Vargas, A., Anderson, D.: A comparison of closed-loop performance of multirotor configurations using non-linear dynamic inversion control. Aerospace **2**(2), 325–352 (2015)
50. Bajodah, A.H.: Generalised dynamic inversion spacecraft control design methodologies. IET Control Theory Appl. **3**(2), 239–251 (2009)
51. Bajodah, A.H.: Asymptotic generalized dynamic inversion attitude control. IET Control Theory Appl. **4**(5), 827–840 (2010)
52. Hameduddin, I., Bajodah, A.H.: Nonlinear generalised dynamic inversion for aircraft manoeuvring control. Int. J. Control **85**(4), 437–450 (2012)
53. Bajodah, A.H.: Asymptotic perturbed feedback linearization of under actuated Euler's dynamics. Int. J. Control **82**(10), 1856–1869 (2009)
54. Hall, J., Romano, M., Cristi, R.: Quaternion feedback regulator for large angle maneuvers of underactuated spacecraft. In: American Control Conference, Baltimore, MD, USA, pp. 2867–2872 (2010)
55. Gui, H., Jin, L., Xu, S.: Attitude control of a rigid spacecraft with one variable speed control moment gyro. Acta Mech. Sin. **29**(5), 749–760 (2013)
56. Gui, H., Jin, L., Xu, S.: Attitude maneuver control of a two-wheeled spacecraft with bounded wheel speeds. Acta Astronaut. **88**, 98–107 (2013)
57. Leishman, J.G.: Principles of Helicopter Aerodynamics, 2nd edn. Cambridge University Press, Cambridge (2002)
58. Nelson, R.C.: Flight Stability and Automatic Control, 2nd edn. McGraw-Hill, New York (1998)
59. Kasdin, N.J., Paley, D.A.: Engineering Dynamics. Princeton University Press, Princeton (2011)
60. Khalil, H.K.: Nonlinear Systems. Prentice-Hall, New Jersey (1996)